Inorganic Chemistry

pubs.acs.org/IC

Forum Article

O_2 Activation with a Sterically Encumbered, Oxygen-Deficient Polyoxovanadate-Alkoxide Cluster

Rachel L. Meyer, Pere Miró, William W. Brennessel, and Ellen M. Matson*

Cite This: *Inorg. Chem.* 2021, 60, 13833−13843

Read Online

ABSTRACT: The isolation of the oxygen-deficient, polyoxovanadate-alkoxide (POV-alkoxide) cluster, [^{n}Bu$_4$N][V$_6$O$_6$(OMe)$_{12}$(MeCN)], and its subsequent reactivity with oxygen (O_2), has demonstrated the utility of these assemblies as molecular models for heterogeneous metal oxide catalysts. However, the mechanism through which this cluster activates and reduces O_2 to generate the oxygenated species is poorly understood. Currently it is speculated that this POV-alkoxide mediates the four-electron O−O bond cleavage through an O_2 bridged dimeric intermediate, a mechanism which is not viable for O_2 reduction at solid-state metal oxide surfaces. Here, we report the successful activation and reduction of O_2 by the calix-functionalized POV-alkoxide cluster, [^{n}Bu$_4$N][(calix)V$_6$O$_6$(OMe)$_8$](MeCN)] (calix = 4-*tert*-butylcalix[4]-arene). The steric hindrance imparted to the open vanadium site by the calix motif eliminates the possibility of cooperative, bimolecular O_2 activation, allowing for a comparison of the reactivity of this system with that of the nonfunctionalized POV-alkoxide described previously. Rigorous characterization of the calix-substituted assembly, enabled by its newfound solubility in organic solvent, reveals that the incorporation of the tetradentate aryloxide ligand into the POV-alkoxide scaffold perturbs the electronic communication between the site-differentiated vanadium(III) ion and the cluster core. Collectively, our results provide insight into the physiochemical factors that are important during the O_2 reduction reaction at oxygen-deficient sites in reduced POV-alkoxide clusters.

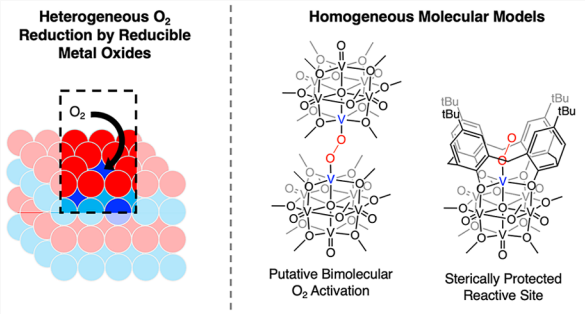

Modeling heterogeneous O_2 activation with a sterically-encumbered, oxygen-deficient polyoxovanadate-alkoxide

■ INTRODUCTION

The abundant, natural supply of dioxygen (O_2), coupled with its atom economy and benign byproduct (e.g., H_2O), renders this small molecule an attractive terminal oxidant.[1−4] Indeed, both natural (e.g., cellular respiration)[5] and anthropogenic (e.g., combustion, fuel cells)[6,7] processes exploit the favorable thermodynamic driving force of the O_2 reduction to water half-reaction. However, while O_2 reduction is exergonic, there are significant kinetic barriers associated with the activation of this small molecule.[8] As such, catalysts capable of mediating the activation of O_2 are essential for facilitating its reactivity. Currently, the vast majority of oxygen reduction catalysts used industrially take advantage of precious metals, such as platinum and palladium.[3,4,9−11] The limited supply of these metals makes them impractical for long-term use on industrial scales.

Reducible metal oxides (RMOs) have shown promise in catalyzing oxidation reactions with O_2.[12−16] The redox flexibility of the metals contained within these RMO materials allows them to support an array of multielectron, multiproton transformations.[17,18] A variety of mechanisms have been reported for RMO-mediated O_2 reduction reactions. RMOs are capable of activating O_2 through outer-sphere electron transfer and/or proton coupled electron transfer reactions, resulting in the formation of the superoxide radical anion ($O_2^{\bullet-}$) or hydrogen peroxide (H_2O_2), respectively.[8,12,19,20] However, these radical pathways tend to be unselective in product formation, rendering inner-sphere O_2 activation mechanisms desirable. One such inner-sphere route of substrate oxidation by RMOs proceeds through the Mars-van-Krevelen (MvK) mechanism.[21,22] In this mechanism, the substrate reacts with the RMO surface, resulting in substrate oxidation via O atom transfer and the formation of an oxygen-atom vacancy at the surface of the material. The resultant, reduced metal site can then activate oxygenated substrates, like O_2, to regenerate the active form of the catalyst. This spatiotemporal separation of substrate oxidation and subsequent reduction of molecular oxygen of the MvK mechanism is vital, as it allows for increased product selectivity over the alternative radical-driven processes (e.g., autoxidation).[8]

Although the MvK mechanism is well-accepted in RMO catalysis, limitations of *in situ* spectroscopic analyses of these heterogeneous systems have inhibited progress in the direct

Special Issue: Advances in Small-Molecule Activation

Received: March 22, 2021
Published: June 23, 2021

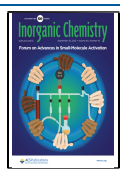

https://doi.org/10.1021/acs.inorgchem.1c00887
Inorg. Chem. 2021, 60, 13833−13843

experimental observation of the proposed reactivity at the surface of metal oxides.[21−24] This is often complicated by the fact that reoxidation of the metal-oxide surface (passivation of O atom defects) is kinetically rapid, rendering the formation of isurface activation intermediates challenging to observe. As a result, researchers have turned to theoretical investigations to probe the energy landscape of the reactivity of O_2 with O atom vacancies in these materials.[25−30] An alternative and increasingly popular approach uses homogeneous molecular models. These soluble, metal oxide assemblies can provide valuable, atomistic insight into the surface reactivity of bulk solids.

Polyoxometalates (POMs) are discrete metal-oxide assemblies that display similar structural and electronic characteristics to that of bulk systems.[31−35] As such, POMs have emerged as homogeneous analogues to RMOs. Indeed, these clusters have demonstrated catalytic activity toward the aerobic oxidation of a variety of substrates invoked in heterogeneous catalytic systems.[36−43] Extensive kinetic and theoretical studies have established that O_2 reduction in these systems typically proceeds through outer-sphere electron transfer mechanisms.[43−46] This is credited to the fact that the oxide-terminated surfaces of these metal oxide assemblies inhibit direct interaction of O_2 with reduced transition metal centers within the cluster. A notable exception, however, is the Keggin-type, phosphovanadomolybdate cluster, $H_5PV_2Mo_{10}O_{40}$, where the coordinatively flexible vanadium centers are purported to serve as the location of inner-sphere reactivity with O_2.[47−51]

In 2018, our laboratory reported the synthesis of an oxygen-deficient, polyoxovanadate-alkoxide (POV-alkoxide) cluster, $[^nBu_4N][V_6O_6(OMe)_{12}(MeCN)]$ ($V_6O_6^{-1}$; Figure 1).[52] This oxygen atom vacancy-containing cluster was accessed directly via treatment of the fully oxygenated Lindqvist ion, $[^nBu_4N][V_6O_7(OMe)_{12}]$ ($V_6O_7^{-1}$), with vanadium(III) trismesityl. Scission of a single $V^V{=}O$ bond results in the generation of a site-differentiated V^{III} center at the surface of the assembly. Complex $V_6O_6^{-1}$ presents a structural and functional homogeneous model for O atom defects at the surface of reducible metal oxides. Isolation of this oxygen-deficient vanadium oxide assembly on preparative scales allows for defect formation and subsequent reactivity to be probed separately. Toward this goal, our laboratory has investigated the reactivity of these oxygen-deficient assemblies; we reported activation of nitrite and nitrate by $V_6O_6^{-1}$, whereby oxygen atom transfer to the surface of the cluster from the oxyanion results in the formation of NO.[53,54] We have also described the reactivity of the oxygen-deficient POV-alkoxide with O_2; exposure of $V_6O_6^{-1}$ to O_2 afforded quantitative formation of the fully oxygenated parent cluster, $V_6O_7^{-1}$.[52] In the latter study, we proposed that O_2 activation by $V_6O_6^{-1}$ proceeds via a multicluster substrate activation pathway; two vanadium(III) centers bind to opposite ends of O_2, each providing two reducing equivalents for the complete cleavage of the O═O bond. This bimolecular, four-electron O_2 activation pathway is consistent with mechanisms reported for other established, homogeneous mononuclear V(III) complexes.[55−57]

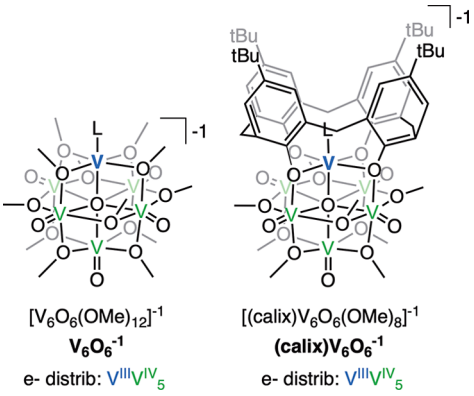

Figure 1. Discrepancies in the molecular structures of POV-alkoxide clusters studied in this work.

While the aforementioned mechanism of O_2 activation by $V_6O_6^{-1}$ is attractive from an atom-economy perspective, there is no experimental proof supporting its validity. In the absence of rigorous kinetic data, we sought to narrow down the possible mechanistic routes via synthetic means. Specifically, we postulated that by increasing the steric bulk around the reactive V(III) center we would eliminate the ability of two, distinct, oxygen-atom-deficient POV-alkoxide clusters to engage in cooperative O_2 binding and activation (Figure 1). In addition to providing insight into the possible mechanism of O_2 activation with POV-alkoxide clusters, the inhibition of cluster dimerization for small molecule activation would increase the efficacy of our models for substrate activation in heterogeneous systems, as bimolecular pathways for O_2 activation are inaccessible in the solid state.

Here, we report our investigations into the synthesis, characterization, and reactivity of an organosoluble version of the calix-functionalized, Lindqvist-type POV-alkoxide cluster, $[^nBu_4N][(calix)V_6O_6(OMe)_8(MeCN)]$ (calix = 4-*tert*-butylcalix[4]arene) with O_2 (Figure 1). This modified version of the cluster was selected because the bulky calix ligand surrounding the oxygen-deficient V(III) moiety inhibits traditional pathways of bimolecular, four electron O_2 activation outlined above. Thus, reaction of the cluster with O_2 must proceed through an alternate reaction pathway. Overall, these studies offer insight into the mechanisms through which oxygen-deficient POV-alkoxide clusters reduce molecular oxygen, which has implications in the use of these POV-alkoxides as RMO models, as well as oxidation catalysts in their own right.

■ RESULTS AND DISCUSSION

Synthesis and Characterization of $[^nBu_4N][(calix)V_6O_6(OMe)_8(MeCN)]$. Interested in studying the reactivity of O_2 at a single, oxygen deficient vanadium center through the elimination of multicluster cooperative small molecule activation pathways, we set out to investigate the reactivity of a calix-substituted variant of the Lindqvist ion. As described above, previous work from Luneau and co-workers established the synthesis of the desired reduced vanadium oxide assemblies, noting the stabilization of an oxygen-deficient vanadium ion within the cavity of the organofunctionalized assembly (Figure 1).[58] Calix-functionalized transition metal complexes have been used in similar studies focused on isolating small molecule activation to a single metal ion; appending these macrocyclic moieties to the secondary coordination sphere of a transition metal complex results in the formation of a bulky, hydrophobic cavity that tunes the selectivity of small molecule activation.[59−61] Of particular relevance to the work presented here, Reinaud and co-workers have reported the reactivity of copper variants of calix-functionalized, funnel-type complexes with O_2, illustrating the

https://doi.org/10.1021/acs.inorgchem.1c00887
Inorg. Chem. 2021, 60, 13833−13843

Scheme 1. Synthesis of an Organosoluble Variant of calixV$_6$O$_6^{-1}$

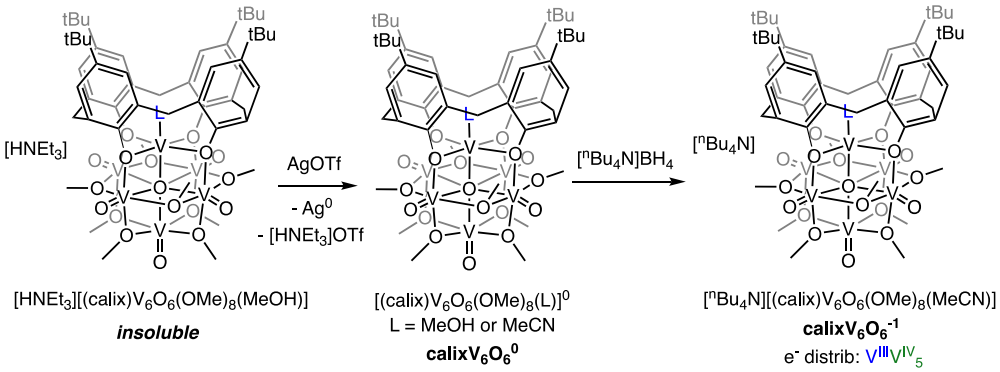

propensity of this bulky substituent to prevent the traditionally observed bimolecular activation of the small molecule upon coordination to the reduced transition metal ion.[62,63] Density functional calculations on a model system were used to assess the validity of our hypothesis that the calix ring would eliminate the possibility of a bimolecular pathway for O_2 activation in the case of the organofunctionalized POV-alkoxide cluster; in the equilibrium geometry of the dimeric species, the distance between vanadium active sites is 11.1 Å. Forcing the clusters to move closer together is energetically unfavorable due to the steric repulsion of the calix groups (Figure S1, see Supporting Information for additional details). Collectively, literature precedent and our theoretical analysis confirm our assumption that the calix-substituted derivative of the POV-alkoxide ion would render multicluster cooperative O_2 activation inaccessible.

The previously reported [cation][(calix)-V$_6$O$_6$(OMe)$_8$(MeOH)] (cation = HNEt$_3$, NEt$_4$, pyridinium) complexes are accessed by heating a mixture of calix pro-ligand and vanadyl sulfate, with the appropriate base, in methanol at 170 °C.[58] Unfortunately, the cluster products from these solvothermal reactions are insoluble in organic solvent, rendering them incompatible with the *homogeneous* small molecule activation studies required for direct comparison of the reactivity of the bulky derivative with the noncalix-functionalized assemblies. Thus, we sought to generate organosoluble variants via cation substitution.

Our initial attempts to generate the tetrabutylammonium salt of the monoanionic calix-functionalized POV-alkoxide cluster involved stirring a suspension of [HNEt$_3$][(calix)-V$_6$O$_6$(OMe)$_8$(MeOH)] with an excess of tetrabutylammonium hexafluorophosphate (acetonitrile, 70 °C, 24 h). However, salt metathesis provided no conversion from the starting material. Thus, we explored a stepwise approach to cation exchange via sequential oxidation and reduction of the hexavanadate assembly (Scheme 1). Oxidation of [HNEt$_3$][(calix)-V$_6$O$_6$(OMe)$_8$(MeOH)] with one equivalent of silver triflate in dichloromethane afforded a golden-brown solution and precipitation of Ag^0 (Scheme 1). The purported neutral species, [(calix)V$_6$O$_6$(OMe)$_8$(MeCN)] (calixV$_6$O$_6^0$), was isolated by extraction with diethyl ether (81% yield); sample purity was confirmed by ^{1}H NMR spectroscopy (CDCl$_3$, Figure S2) and elemental analysis. To generate the desired reduced assembly, tetrabutylammonium borohydride ([^{n}Bu$_4$N]BH$_4$) was added to a tetrahydrofuran solution of calixV$_6$O$_6^0$. Following workup, the product, [^{n}Bu$_4$N][(calix)-V$_6$O$_6$(OMe)$_8$](MeOH)] (calixV$_6$O$_6^{-1}$), was isolated as a brown solid in good yield (71%). Notably, calixV$_6$O$_6^{-1}$ exhibited improved solubility in polar organic solvents.

Initial characterization of calixV$_6$O$_6^{-1}$ was performed by ^{1}H NMR spectroscopy (CDCl$_3$, Figure S3). The spectrum of calixV$_6$O$_6^{-1}$ revealed two prominent, paramagnetically shifted and broadened resonances at 27.1 (12 H) and 23.6 (12 H) ppm, assigned to the two chemically inequivalent groups of bridging methoxide ligands. This observation is consistent with the expected C_{4v} symmetry of this molecule. An additional broad resonance was noted at 17.6 ppm and assigned to the methanol solvent molecule bound to the oxygen-deficient, V(III) center. Resonances attributed to the protons of the calix ligand were observed at 8.7 (8 H, arene C−H moieties) and 1.2 (44 H, *tert*-butyl moieties). Electrospray ionization-mass spectrometry (ESI-MS) of calixV$_6$O$_6^{-1}$ contained signals for the expected oxygen-deficient assembly (1294 *m*/*z*, [(calix)-V$_6$O$_6$(OMe)$_8$]$^{-1}$; 1326 *m*/*z*, [(calix)-V$_6$O$_6$(OMe)$_8$(MeOH)]$^{-1}$; 1335 *m*/*z*, [(calix)-V$_6$O$_6$(OMe)$_8$(MeCN)]$^{-1}$; Figure S4). Bulk sample purity was ultimately verified by elemental analysis.

To unambiguously confirm formation of calixV$_6$O$_6^{-1}$, crystals suitable for single crystal X-ray diffraction (SCXRD) were grown from diffusion of diethyl ether into a concentrated acetonitrile solution (Figure 2, Table 1; see Table S1 for complete crystallographic data and refinement parameters). Following structural refinement, the expected calix-functionalized, oxygen-deficient Lindqvist assembly was observed. Broadly speaking, the molecular structure of calixV$_6$O$_6^{-1}$

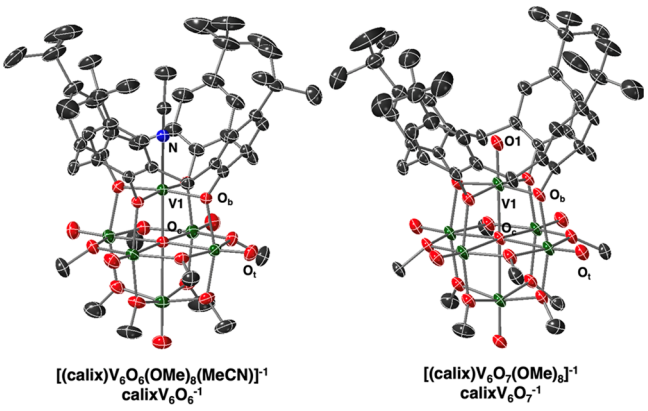

Figure 2. Molecular structures of calixV$_6$O$_6^{-1}$ and calixV$_6$O$_7^{-1}$ shown with 30% probability ellipsoids. Hydrogen atoms, solvent molecules, and counterions have been omitted for clarity. Key: C, black; N, blue; O, red; V, dark green.

https://doi.org/10.1021/acs.inorgchem.1c00887
Inorg. Chem. 2021, 60, 13833−13843

Table 1. Selected Bond Lengths of calix$V_6O_6^{-1}$ and calix$V_6O_7^{-1}$

bond	calix$V_6O_6^{-1}$[a]	calix$V_6O_7^{-1}$
V1−N_{MeCN}	2.131(3) Å	
V1=O_t[b]		1.610(3) Å
V1−O_c[c]	2.037(2) Å	2.107(3) Å
V1−O_b(calix)[d] (avg)	1.9491 Å	1.930 Å
V_n=O_t[b,e] (avg)	1.592 Å	1.598 Å
V_n−O_c[b,c] (avg)	2.361 Å	2.358 Å
V_n−O_b(calix)[b,e] (avg)	2.0458 Å	2.061 Å
V_n−O_b(OMe)[b,e] (avg)	1.9987 Å	2.000 Å

[a]Bond metrics described in Table 1 refer to those collected for the acetonitrile adduct of monoanionic, calix-functionalized POV-alkoxide cluster reported in this work. [b]O_t = terminal oxygen atom. [c]O_c = central m_6-oxygen atom. [d]O_b = oxygen atom of bridging aryl/alkoxide ligands. [e]n = V2−V6.

closely resembles those of the analogous assemblies reported by Luneau, [cation][(calix)V_6O_6(OMe)$_8$(MeOH)] (cation = $HNEt_3$, NEt_4, pyridinium).[58] However, the enhanced solubility of calix$V_6O_6^{-1}$ following cation substitution affords opportunities to crystallize the assembly under conditions different from those previously reported. This results in isolation of a calix-functionalized POV-alkoxide cluster with an acetonitrile molecule bound to the reduced vanadium center (note: in the original structures, methanol was coordinated to this assembly). This observation demonstrates the lability of the solvent molecule at the defect site.

Analysis of the bond metrics of V1 in the molecular structure of calix$V_6O_6^{-1}$ reveals unique structural parameters for the site differentiated vanadium center. V1 adopts a pseudo-octahedral coordination environment, with the four phenoxide moieties of the calix ligand composing the equatorial plane of the octahedron (average V1−O_b bond distance of 1.9491 Å). The V1−O_b lengths are slightly elongated in comparison to previously reported mononuclear molecular structures of calix-ligated V(III) compounds (1.807(2)−1.841(5) Å).[64] This is attributed to the bridging character of the phenoxide oxygen atoms. It is interesting to note that the V1−O_b bond distances are slightly shorter than the Vn−O_b distances (n = 2, 3, 4) of the vanadium centers that compose the remainder of the Lindqvist structure, suggesting that the calix ligand enforces a strict coordination environment at V1. The V1−O_c (O_c = μ_6-central oxygen atom) distance is substantially shortened in comparison to other Vn−O_c bond lengths within the cluster (Vn−O_c (avg) = 2.361 Å). This observation is consistent with the structural reorganization previously reported by our group upon O atom vacancy formation in POV-alkoxide clusters.[52,65,66] It is important to note that substitution of the datively bound methanol solvent molecule for acetonitrile in the calix$V_6O_6^{-1}$ variant reported here has no structural consequences on the coordination environment of the V(III) center (e.g., similar V1−O_c and V1−O_b bond distances reported for all compounds).

Each chemically distinct vanadium center within complex calix$V_6O_6^{-1}$ crystallizes in a unique position, providing us with the opportunity to interrogate the oxidation state distribution of vanadium ions across the Lindqvist core using bond valence sum (BVS) calculations (Table S2). Bond metric analysis of V1 confirms its assignment as a V(III) center; all other vanadyl ions within the cluster more aptly resemble metal ions in their tetravalent oxidation state. This assignment of oxidation states of individual vanadium centers in calix$V_6O_6^{-1}$ ($V^{III}V^{IV}_5$) is consistent with that reported by Luneau et al.[58] Notably, the oxidation state distribution of calix$V_6O_6^{-1}$ mirrors that reported for the nonfunctionalized, POV-alkoxide cluster, $V_6O_6^{-1}$ ($V^{III}V^{IV}_5$).[52]

Prior to evaluating the reactivity of calix$V_6O_6^{-1}$ with O_2, we sought to compare the electronic structure of the POV-alkoxide cluster with that of $V_6O_6^{-1}$. These investigations serve as an important basis for evaluating similarities and differences in the reactivity of these distinct, oxygen-deficient assemblies. Toward this goal, the electronic properties of calix$V_6O_6^{-1}$ were interrogated via infrared (IR) and electronic absorption spectroscopies (Table 2, Figures 3 and 4). These two

Table 2. Select Infrared Data for Complexes $V_6O_6^{-1}$, calix$V_6O_6^{-1}$, $V_6O_7^{-1}$, and calix$V_6O_7^{-1}$

compound	ox. state distrib.	ν(O_b−Me), cm^{-1}	ν(V=O_t), cm^{-1}	($\Delta\nu$), cm^{-1}
calix$V_6O_6^{-1}$	$V^{III}V^{IV}_5$	1051	960	91
$V_6O_6^{-1}$	$V^{III}V^{IV}_5$	1047	951	96
calix$V_6O_7^{-1}$	$V^{IV}_5V^{V}$	1051	961	90
$V_6O_7^{-1}$	$V^{IV}_5V^{V}$	1026	953	73

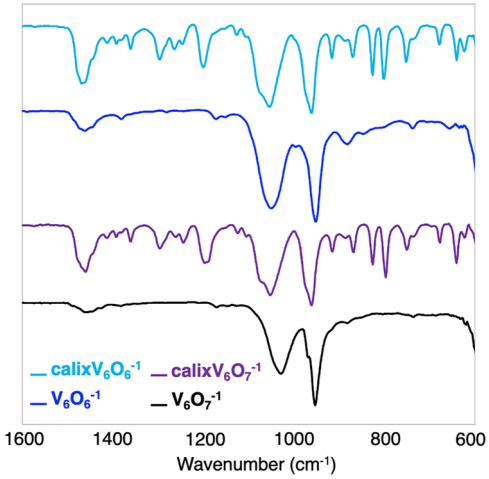

Figure 3. Infrared spectra of complexes $V_6O_6^{-1}$, calix$V_6O_6^{-1}$, $V_6O_7^{-1}$, and calix$V_6O_7^{-1}$.

techniques, taken in tandem, have been demonstrated to report on the degree of reduction of the cluster core.[52,54,65,67−70] IR analysis of calix$V_6O_6^{-1}$ reveals transitions at 1051 and 960 cm^{-1}, assigned to ν(O_b−Me) and ν(V=O_t), respectively (Table 2, Figure 3). These values are shifted from those reported for $V_6O_6^{-1}$ (ν(O_b−Me) = 1047 cm^{-1}; ν(V=O_t) = 951 cm^{-1})[52] and exhibit significant shouldering, likely due to the incorporation of the calix ligand at the surface of the assembly. The energy difference between the ν(O_b−Me) and ν(V=O_t) vibrations ($\Delta\nu$) has been shown to inform the degree of reduction within the Lindqvist core.[65] The $\Delta\nu$ values for calix$V_6O_6^{-1}$ (91 cm^{-1}) and $V_6O_6^{-1}$ (96 cm^{-1}) are similar, suggesting that the degree of reduction of the two cluster assemblies is comparable.

The electronic absorption spectrum of calix$V_6O_6^{-1}$ is similar to that previously reported for $V_6O_6^{-1}$ (Figure 4). For the calix-functionalized derivative, a low intensity absorption feature is observed at 520 nm (ε = 200 M^{-1} cm^{-1}), which is assigned to a V^{IV} d→d transition.[52,68] This band is shifted

https://doi.org/10.1021/acs.inorgchem.1c00887
Inorg. Chem. 2021, 60, 13833−13843

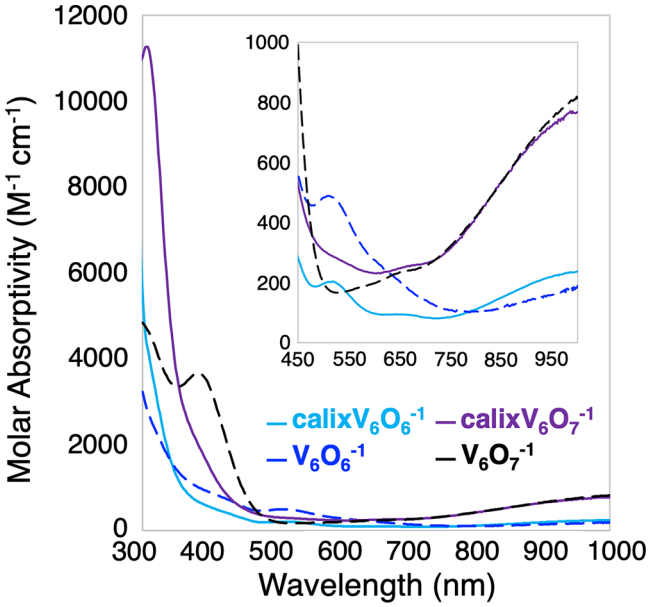

Figure 4. Electronic absorption spectra of complexes $V_6O_6^{-1}$, calix$V_6O_6^{-1}$, $V_6O_7^{-1}$, and calix$V_6O_7^{-1}$ collected in acetonitrile at 21 °C. Inset highlights the low-energy region of the spectra to clearly illustrate the IVCT bands.

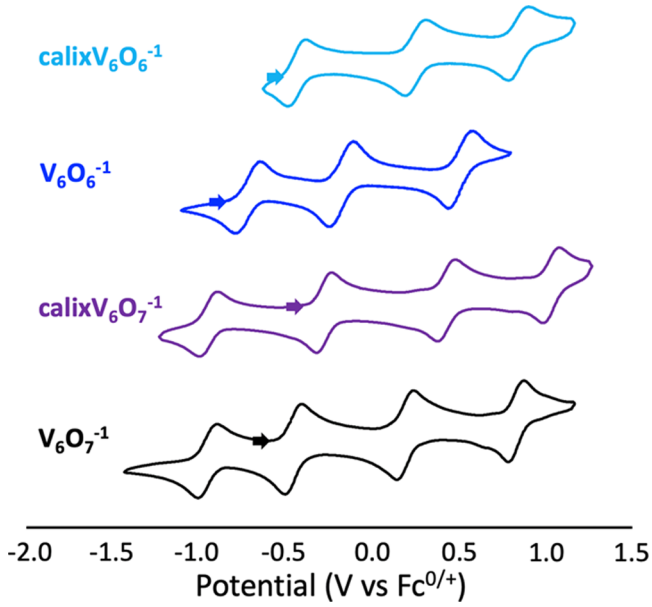

Figure 5. Cyclic voltammogram of complexes calix$V_6O_6^{-1}$ (light blue, top), $V_6O_6^{-1}$ (dark blue), calix$V_6O_7^{-1}$(purple), and $V_6O_7^{-1}$ (black, bottom) collected in dichloromethane (supporting electrolyte = 0.1 M [^{n}Bu$_4$N]PF$_6$; potentials referenced to Fc$^{+/0}$). The locations of the open circuit potentials and scan direction of each sample are indicated by arrows.

slightly to higher energies in comparison to the corresponding signal reported for complex $V_6O_6^{-1}$ (λ = 526 nm, ε = 470 M^{-1} cm^{-1}),[52] which we attribute to the increased electron withdrawing character of the phenoxide moieties of the calix ligand. Collectively, these data are consistent with the oxidation state distribution of calix$V_6O_6^{-1}$ determined from BVS calculations and qualify the assembly as electronically similar to that of $V_6O_6^{-1}$.

Further insight into the electronic properties of calix$V_6O_6^{-1}$ was obtained using electrochemical characterization of the redox active vanadium oxide assembly. The cyclic voltammogram (CV) of calix$V_6O_6^{-1}$ was collected in dichloromethane (Figure 5, Table 3). Generally speaking, the redox profile of the calix-substituted, oxygen-deficient assembly is similar to that of $V_6O_6^{-1}$. Calix$V_6O_6^{-1}$ possesses three quasi-reversible redox events at −0.42, +0.26, and +0.86 V (vs Fc$^{+/0}$) with an open circuit potential (OCP) located at −0.54 V vs Fc$^{+/0}$, suggesting this cluster is isolated in its most reduced state. Peak-to-peak separation ($\Delta E_{1/2}$) of individual redox processes of 0.60 and 0.68 V, corresponding to comproportionation constants ranging from 2.1 × 10^{10} to 5.0 × 10^{11} (comproportionation constants were determined through the following calculation: $RT \ln K_c = nF[DE_p]$),[71−73] are consistent with those reported previously for $V_6O_6^{-1}$ (K_c = 5.5 × 10^9 to 9.4 × 10^{11}).[52] One notable difference, however, between the voltammograms of the two clusters is that the potential of the electrochemical processes of calix$V_6O_6^{-1}$ are shifted anodically from that of $V_6O_6^{-1}$ by ∼0.35 V. We attribute this substantial shift to the electron-accepting properties of the calix phenoxide moieties,[74−77] which destabilize oxidation of the cluster core. This anodic shift is important in the context of O_2 reduction, as the thermodynamics of electron transfer of calix$V_6O_6^{-1}$ are significantly attenuated relative to $V_6O_6^{-1}$.

Reactivity of calix$V_6O_6^{-1}$ with O_2. The isolation of oxygen-deficient POV-alkoxide clusters allows for inner sphere, MvK-type mechanisms of small molecule activation to be invoked.[53,54,66] In our original report of defect formation in POV-alkoxide clusters, we described the quantitative conversion of $V_6O_6^{-1}$ to the fully oxygenated product, $V_6O_7^{-1}$, upon addition of O_2.[52] As described above, we proposed that O_2 activation proceeds through a bimolecular pathway, where the vanadium(III) centers of two POV-alkoxide clusters attack opposite ends of the O_2 molecule, each contributing two electrons to facilitate the cleavage of the O═O bond. However, no experimental evidence was provided to support this hypothesis. Thus, to interrogate the validity of a bimolecular pathway for O_2, we set out to compare the reactivity of calix$V_6O_6^{-1}$ with O_2 to that reported for the $V_6O_6^{-1}$ system.

Table 3. Half-Wave Potential ($E_{1/2}$) Values of the Redox Couples Observed in Complexes $V_6O_6^{-1}$, calix$V_6O_6^{-1}$, $V_6O_7^{-1}$, and calix$V_6O_7^{-1}$ in Dichloromethane

redox couple	$E_{1/2}$ (V)[a] $V_6O_6^{-1}$	$E_{1/2}$ (V)[a] calix$V_6O_6^{-1}$	redox couple	$E_{1/2}$ (V)[a] $V_6O_7^{-1}$	$E_{1/2}$ (V)[a] calix$V_6O_7^{-1}$
$[V^{III}V^{IV}_5]/[V^{III}V^{IV}_4V^V]$	−0.70	−0.42	$[V^{IV}_6]/[V^{IV}_5V^V]$	−0.94	−0.94
$[V^{III}V^{IV}_4V^V]/[V^{III}V^{IV}_3V^V_2]$	−0.16	+0.26	$[V^{IV}_5V^V]/[V^{IV}_4V^V_2]$	−0.45	−0.27
$[V^{III}V^{IV}_3V^V_2]/[V^{III}V^{IV}_2V^V_3]$	+0.52	+0.86	$[V^{IV}_4V^V_2]/[V^{IV}_3V^V_3]$	+0.20	+0.44
$[V^{III}V^{IV}_2V^V_3]/[V^{III}V^{IV}_1V^V_4]$			$[V^{IV}_3V^V_3]/[V^{IV}_2V^V_4]$	+0.84	+1.06

[a]All $E_{1/2}$ values are reported on the basis of data collected in dichloromethane and referenced vs Fc$^{+/0}$.

https://doi.org/10.1021/acs.inorgchem.1c00887
Inorg. Chem. 2021, 60, 13833−13843

To directly compare the established results of O_2 activation with the sterically unencumbered, oxygen-deficient POV-alkoxide cluster to the bulky, calix-functionalized assembly, we attempted the addition of O_2 to calix$V_6O_6^{-1}$ following identical reaction conditions reported for the oxidation of $V_6O_6^{-1}$. Exposure of O_2 to an acetonitrile solution of calix$V_6O_6^{-1}$ resulted in a gradual darkening of the reaction mixture, consistent with the anticipated oxidation of the cluster core. Analysis of the crude reaction mixture by ^{1}H NMR spectroscopy revealed a mixture of products (Figure S5); five paramagnetically shifted and broadened resonances are observed (δ = 33.9, 27.4, 23.6, 22.0, 15.5 ppm). The signals located at 33.9 and 15.5 ppm correspond to the protons of the bridging methoxide ligands of the calix$V_6O_6^0$ cluster (*vide supra*). To further simplify characterization efforts of the O_2 reaction products and to quantitate the yield of calix$V_6O_6^0$, the neutral calix-functionalized cluster was separated from the other monoanionic products via extraction into diethyl ether; characterization of the extracted product confirmed the successful isolation of calix$V_6O_6^0$ from the crude reaction mixture (Figure S5, 28% yield based on calix$V_6O_6^{-1}$). ^{1}H NMR analysis of the remaining solid revealed three additional resonances (Figure S7), two of which appear to belong to unreacted calix$V_6O_6^{-1}$ (δ_{OMe} = 27.1 and 23.6 ppm). The final, broad signal is observed, attributed to an unidentified product of the reaction.

We hypothesized that the new product observed after exposure of calix$V_6O_6^{-1}$ to O_2 might be the fully oxygenated species, [^{n}Bu$_4$N][(calix)V_6O_7(OMe)$_8$] (calix$V_6O_7^{-1}$). Thus, to further explore the possibility of oxygenation of calix$V_6O_6^{-1}$ in the presence of O_2, we sought to independently synthesize calix$V_6O_7^{-1}$. Treatment of calix$V_6O_6^{-1}$ with an excess of iodosylbenzene (PhIO) in dichloromethane resulted in a gradual darkening of the brown reaction mixture (Scheme 2).

Scheme 2. Independent Synthesis of calix$V_6O_7^{-1}$ with Iodosylbenzene (PhIO)

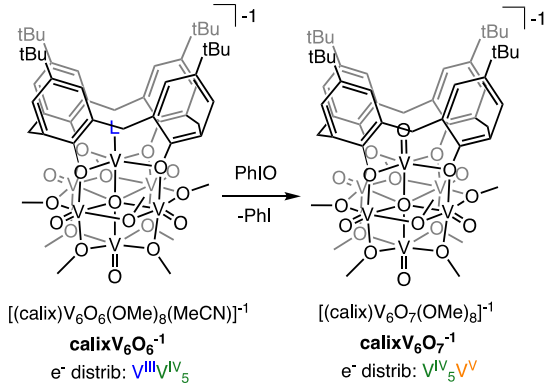

Analysis of the ^{1}H NMR spectrum of the crude reaction revealed a mixture of calix$V_6O_6^0$ and a second species with broad resonances, similar to those described above in the crude reaction of calix$V_6O_6^{-1}$ with O_2 (δ_{OMe} = 28.0, 23.6, and 21.5 ppm; Figure S8). The molecular composition of the second species was confirmed as calix$V_6O_7^{-1}$ by ESI-MS (1310 m/z, [(calix)V_6O_7(OMe)$_8$]$^{-1}$; Figure S9). Following workup, calix$V_6O_7^{-1}$ was isolated as a brown-green solid in good yield (65%; ^{1}H NMR of analytically pure product shown in Figure S10).

The molecular structure of calix$V_6O_7^{-1}$ was confirmed by X-ray diffraction of crystals grown from diffusion of toluene into a saturated dichloromethane solution (Figure 2, Table 1). The molecular structure resembles that of calix$V_6O_6^{-1}$, with the notable exception of the fact that the solvent molecule in the starting material bound to the oxygen-deficient site of the V1 ion has been replaced by a terminal oxido ligand. The new V1−O1 bond distance (1.610(3) Å) is slightly elongated in comparison to the remaining Vn−O_t lengths of the structure (avg. 1.598 Å) but compares favorably with values previously reported for mononuclear V(V) oxo complexes (1.5816(14)−1.6055(14) Å).[78−82] Oxidation of V1 translates to an elongation of the V1−O_c bond in calix$V_6O_7^{-1}$ (2.107(3) Å), as compared to calix$V_6O_6^{-1}$ (2.037(2) Å). The V1−O_c bond length is considerably shorter than other Vn−O_c bonds in the cluster (avg. 2.358 Å), highlighting the unique coordination environment of the site differentiated vanadium center within the Lindqvist ion. The V1−O_b distances of 1.930 Å are elongated from those reported previously for mononuclear, calix-ligated V(V) complexes (1.8858(4) Å),[83] once again attributed to the bridging nature of the phenoxide moieties within the polynuclear assembly.

Each vanadium center within the Lindqvist core was refined in a crystallographically unique position, allowing for BVS calculations to be employed to verify the oxidation state distribution of the vanadium oxide cluster (Table S3). Bond metric analysis of V1 reveals that this metal center is oxidized to the pentavalent oxidation state upon the addition of PhIO, consistent with the expected two-electron oxidation of the metal center following oxygen atom transfer. All remaining vanadyl ions retain their tetravalent oxidation states, resulting in an overall oxidation state distribution for calix$V_6O_7^{-1}$ of $V^{IV}{}_5V^V$. This assignment of formal oxidation states of vanadium centers within the oxidized product resembles that reported for the nonfunctionalized, monoanionic POV-alkoxide cluster, $V_6O_7^{-1}$ ($V^{IV}{}_5V^V$).[68,70,84]

The cyclic voltammogram of calix$V_6O_7^{-1}$ collected in dichloromethane contained four redox events at −0.94, −0.27, +0.44, and +1.06 V vs $Fc^{+/0}$ (Figure 5, Table 3). The open circuit potential was measured at −0.4 V, placing the monoanionic charge state of the assembly between the two most reducing redox events. The approximately even spacing between the redox processes ($\Delta E_{1/2}$ = 0.62 to 0.71 V) is similar to that of the calix$V_6O_6^{-1}$ cluster. The comproportionation constants for the oxygenated cluster range from 4.7 × 10^{10} to 1.6 × 10^{12}, indicating that the electronic delocalization within the cluster core is retained upon formation of the V(V)═O unit. The $E_{1/2}$ values of the individual redox events in the electrochemical profile of calix$V_6O_7^{-1}$ are quite similar to that of $V_6O_7^{-1}$ (−0.94, −0.45, +0.20, and +0.84 V vs $Fc^{+/0}$), an average overall anodic shift of 0.16 V relative to $V_6O_7^{-1}$.

The electronic structure of calix$V_6O_7^{-1}$ was further interrogated by IR and electronic absorption spectroscopies (Table 2, Figures 3 and 4). The IR spectrum contained ν(O_b−Me) and ν(V═O_t) located at 1051 and 961 cm^{-1}, respectively. These values are nearly identical to that of the oxygen-deficient assembly, calix$V_6O_6^{-1}$ (ν(O_b−Me) = 1051 cm^{-1}; ν(V═O_t) = 960 cm^{-1}). This observation is in stark contrast to the changes in the IR spectrum of the nonfunctionalized cluster upon oxidation; $V_6O_7^{-1}$ exhibits vibrations at 1026 and 953 cm^{-1}, which are shifted from those of $V_6O_6^{-1}$ (ν(O_b−Me) = 1047 cm^{-1}; ν(V═O_t) = 951 cm^{-1}). The changes in the IR spectra of the two clusters are most notable when comparing the

https://doi.org/10.1021/acs.inorgchem.1c00887
Inorg. Chem. 2021, 60, 13833−13843

energy difference of these two vibrations; in the case of $V_6O_7^{-1}$, the separation between $\nu(O_b-Me)$ and $\nu(V{=}O_t)$ is smaller ($\Delta\nu$ = 73 cm^{-1}) than that of $V_6O_6^{-1}$ ($\Delta\nu$ = 96 cm^{-1}), whereas the difference in bands in the calix-functionalized assemblies remains constant. Similar perturbations of $\Delta\nu$ have been attributed to a variation in electron density contained within the delocalized cluster core upon oxidation of the V(III) center to V(V).[52,65] The observed invariance of the $\nu(O_b-Me)$ and $\nu(V{=}O_t)$ vibrations for calix$V_6O_6^{-1}$ and calix$V_6O_7^{-1}$ suggests that the site differentiation of the apical vanadium enforced by the calix ligand decouples this ion from the remaining vanadium centers of the cluster core.

The electronic absorption spectrum of calix$V_6O_7^{-1}$ is distinct from that of $V_6O_7^{-1}$. Complex calix$V_6O_7^{-1}$ possesses a broad feature centered at ∼1000 nm; this transition is assigned to an intervalence charge transfer (IVCT) event, enabled by the oxidation of a single vanadium center within the Lindqvist core to the pentavalent oxidation state. It is worth noting, however, that the high-energy, partner IVCT band (located at ∼395 nm), observed in all mixed-valent POV-alkoxide clusters as the dominant feature in the visible region, is absent in the spectrum of calix$V_6O_7^{-1}$. Coupled with the IR data described above, the electronic absorption spectrum of calix$V_6O_7^{-1}$ indicates that incorporation of the calix ligand into the POV-alkoxide scaffold perturbs the mode and degree of electronic communication within the Lindqvist core.

With the oxygenated cluster, calix$V_6O_7^{-1}$, fully characterized, the approximate yields of calix$V_6O_7^{-1}$ and calix$V_6O_6^{-1}$ from the reaction of calix$V_6O_6^{-1}$ with O_2 were calculated via electrochemical analysis of the product mixture after calix$V_6O_6^{0}$ was removed. The CV of this product mixture showed the redox events expected for complexes calix$V_6O_7^{-1}$ and calix$V_6O_6^{-1}$ (Figure S10). Comparing the relative peak currents for the redox events of calix$V_6O_7^{-1}$ and calix$V_6O_6^{-1}$ revealed that the composition of the products from the reaction of calix$V_6O_6^{-1}$ with O_2 is as follows: 28% calix$V_6O_6^{0}$, 42% calix$V_6O_7^{-1}$, and 30% calix$V_6O_6^{-1}$ (Table S4).

With the products from the reaction of calix$V_6O_6^{-1}$ with O_2 identified and quantified (Scheme 2), preliminary insights into the reaction mechanism of O_2 at oxygen atom deficient sites in POV-alkoxides can be discussed. Most importantly, our results show that the calix$V_6O_6^{-1}$ is capable of activating O_2, resulting in the formation of the oxygenated assembly, calix$V_6O_7^{-1}$, albeit in modest yields. The discrepancy in the yield of the fully oxygenated assemblies in the case of the calix-bound (42%) and nonfunctionalized (quantitative) assemblies has a significant implication on possible mechanisms of O_2 reduction performed by oxygen-deficient vanadium oxide Lindqvist ions. Our results suggest that O_2 reduction can be accomplished by these POV-alkoxide systems without accessing the purported cooperative bimolecular O_2 reduction mechanism. While the selective formation of $V_6O_7^{-1}$ upon exposure of $V_6O_6^{-1}$ to O_2, relative to the sterically hindered calix$V_6O_6^{-1}$ system, can potentially support a concerted, intramolecular O_2 activation pathway (i.e., the bimolecular O_2 activation invoked in our initial study), this could also arise from the increased accessibility and reducing power of the V(III) center in the nonfunctionalized assembly, allowing for the rapid coordination and consumption of the reduced O_2 species.

■ CONCLUSION

In this work, we have explored the impact steric bulk has on the reduction of O_2 using oxygen-deficient POV-alkoxide clusters. Installation of a sterically encumbered calix-ligand at the surface of the POV-alkoxide cluster results in a distinct chemical environment for the V(III) reactive site, eliminating the possibility of previously proposed mechanisms for bimolecular O_2 activation with similar complexes. The ability of calix$V_6O_6^{-1}$ to reduce O_2 and generate the oxygenated cluster, calix$V_6O_7^{-1}$, suggests that O_2 activation might proceed through alternative *monomolecular* pathways. Overall, these results show that calix$V_6O_6^{-1}$ can act as a good model for the MvK-type substrate activation invoked in bulk RMO systems.

Ongoing research efforts are focused on elucidating the O_2 activation pathways used by $V_6O_6^{-1}$ and calix$V_6O_6^{-1}$ through kinetic analyses, with the goal of understanding the significance of the disparate properties of these assemblies. In particular, identifying how the V(III) active sites in these oxygen-deficient, POV-alkoxides interact with O_2 (and/or reduced O_2 species) and how they are converted to V(V)=O moieties can provide experimental insight at the atomic level into the MvK mechanisms utilized by RMOs during O_2 reduction processes.

■ EXPERIMENTAL SECTION

General Considerations. All manipulations, unless otherwise noted, were carried out in the absence of water and oxygen in a UniLab MBraun inert atmosphere glovebox under a nitrogen atmosphere. Glassware was oven-dried for a minimum of 4 h and cooled in an evacuated antechamber prior to use. Celite 545 (J. T. Baker) was dried in a Schlenk flask for at least 14 h at 150 °C under a vacuum prior to use. Three-Ångstrom molecular sieves (Fisher Scientific) were activated using the same drying method. Anhydrous methanol (99.8%) was purchased from Sigma-Aldrich and stored over 3 Å molecular sieves. Triethylamine was dried and distilled over calcium hydride and stored over 3 Å molecular sieves. All other solvents were dried and deoxygenated on a Glass Contour System (Pure Process Technology, LLC) and stored over activated 3 Å molecular sieves. Silver trifluoromethanesulfonate and tetrabutylammonium borohydride were purchased from Sigma-Aldrich and used as received. Oxygen gas was purchased from Airgas. 4-t-Butylcalix[4]-arene (calix) and $HNEt_3[(calix)V_6O_6(MeOH)(OMe)_8]$ were prepared following reported methods.[58,85]

^{1}H NMR spectra were recorded on a Bruker DPX-400 MHz spectrometer locked on the signal of the deuterated solvent. All chemical shifts were reported relative to the peak of the residual ^{1}H signal in the deuterated solvent. Deuterated solvents were purchased from Cambridge Isotope Laboratories, degassed by three freeze−pump−thaw cycles, and stored over activated 3 Å molecular sieves. Infrared (FT-IR, ATR) spectra were recorded on a Shimadzu IRAffinity-1 Fourier transform infrared spectrophotometer and are reported in wavenumbers (cm^{-1}). Electronic absorption spectra were recorded at room temperature in anhydrous acetonitrile in a sealed 1 cm quartz cuvette with an Agilent Cary 60 UV−vis spectrophotometer. Mass spectrometry analyses were performed on an Advion ExpressionL compact mass spectrophotometer equipped with an electrospray probe and an ion-trap mass analyzer. Direct injection analysis was employed in all cases with a sample solution in acetonitrile. Elemental analyses were performed on a PerkinElmer 2400 Series II Analyzer at the CENTC Elemental Analysis Facility, University of Rochester.

Cyclic voltammetry (CV) measurements were carried out at room temperature in a nitrogen-filled glovebox using a Bio-Logic SP 150 potentiostat/galvanostat and the EC-lab software suite. CVs were recorded using a glassy carbon working electrode (ø = 3.0 mm) and a Pt wire auxiliary electrode, both purchased from CH Instruments, USA. A $Ag^{0/+}$ nonaqueous reference electrode with 0.01 M $AgNO_3$ and 0.05 M $[^nBu_4N]PF_6$ in acetonitrile was purchased from Bio-Logic and used as the reference electrode for all cyclic voltammetry measurements. $[^nBu_4N]PF_6$ was purchased from Sigma-Aldrich, crystallized thrice from ethanol, and stored under a dynamic vacuum.

https://doi.org/10.1021/acs.inorgchem.1c00887
Inorg. Chem. 2021, 60, 13833−13843

The CVs were collected with 1 mM analyte in 0.1 M [^{n}Bu$_4$N]PF$_6$ acetonitrile solutions. All CV measurements were IR compensated at 85% with impedance taken at 100 kHz using the ZIR tool included with the EC-Lab software. All redox events were referenced against the ferrocene/ferrocenium ($Fc^{+/0}$) redox couple.

Synthesis of [(calix)V$_6$O$_6$(OCH$_3$)$_8$(CH$_3$OH)], calixV$_6$O$_6^0$. In a 20 mL scintillation vial, HNEt$_3$[(calix)V$_6$O$_6$(MeOH)(OMe)$_8$] (0.125 g, 0.087 mmol, 1.0 equiv) was suspended in 10 mL of dichloromethane. Silver triflate (0.027 g, 0.10 mmol, 1.1 equiv) was added to the mixture as a solid. The reaction was stirred vigorously at room temperature for 1 h, affording a brown solution and a gray precipitate. Following filtration, the volatiles were removed under reduced pressure. The resulting brown solid was extracted with diethyl ether (10 mL × 3) and filtered. The diethyl ether was removed under reduced pressure, affording calixV$_6$O$_6^0$ as a gold-brown solid (0.094 g, 0.071 mmol, 81%). ^{1}H NMR (400 MHz, CDCl$_3$): δ 34.00 (12 H), 20.55 (MeOH), 15.42 (12 H), 8.67 (arene), 1.19 (−CH$_2$− and *tert*-butyl, 44 H). FT-IR (ATR, cm^{-1}): 1034 (O$_b$−CH$_3$), 980 (V═O$_t$). UV−vis (CH$_3$CN): 394 (ε = 3580), 1000 nm (ε = 680 M^{-1} cm^{-1}). Elemental analysis for C$_{53}$H$_{80}$O$_{19}$V$_6$ (MW = 1326.84 g/mol). Calculated (%): C, 47.98; H, 6.08. Found (%): C, 48.21; H, 6.03.

Synthesis of ^{n}Bu$_4$N[(calix)V$_6$O$_6$(OCH$_3$)$_8$(CH$_3$OH)]·1/2CH$_2$Cl$_2$, calixV$_6$O$_6^{-1}$. In a 20 mL scintillation vial, calixV$_6$O$_6^0$ (0.123 g, 0.093 mmol, 1.0 equiv) was dissolved in 12 mL of tetrahydrofuran. Solid [^{n}Bu$_4$N]BH$_4$ (0.024 g, 0.09 mmol, 1.0 equiv) was added to the solution in small portions with rapid stirring. No obvious color change was noted. The reaction mixture was stirred at room temperature for 1 h. The reaction mixture was filtered over a glass pipet packed with a glass fiber filter paper, and the volatiles of the filtrate were removed under reduced pressure. The resulting brown residue was triturated with a 3:1 mixture of diethyl ether/tetrahydrofuran (8 mL × 3). The remaining solid was extracted with dichloromethane (4 mL) and filtered over a glass pipet packed with a glass fiber filter paper. The dichloromethane was removed under reduced pressure, affording calixV$_6$O$_6^{-1}$ as a brown solid (0.103 g, 0.064 mmol, 71%). Crystals suitable for structural analysis were grown from slow diffusion of diethyl ether into a saturated acetonitrile solution. ^{1}H NMR (400 MHz, CDCl$_3$): δ 27.08 (12 H), 23.60 (12 H), 17.57 (MeOH), 7.44 (arene), 2.68 (TBA), 1.11 (−CH$_2$− and *tert*-butyl). ^{1}H NMR (400 MHz, CD$_3$CN): δ 26.93 (12 H), 24.03 (12 H), 7.57 (arene, 8 H), 3.06 (TBA), 2.64 (TBA), 1.57 (TBA), 1.20 (−CH$_2$− and *tert*-butyl), 0.96 (TBA). FT-IR (ATR, cm^{-1}): 1051 (O$_b$−CH$_3$), 960 (V═O$_t$). UV−vis (CH$_3$CN): 394 (ε = 3580), 1000 nm (ε = 680 M^{-1} cm^{-1}). Elemental analysis for C$_{69}$H$_{116}$NO$_{19}$V$_6$·1/2 CH$_2$Cl$_2$ (MW = 1597.78 g/mol). Calculated (%): C, 52.25; H, 7.38; N, 0.88. Found (%): C, 52.12; H, 7.12; N, 1.12.

Synthesis of ^{n}Bu$_4$N[(calix)V$_6$O$_7$(OCH$_3$)$_8$]·1/2CH$_2$Cl$_2$, calixV$_6$O$_7^{-1}$. A 20 mL scintillation vial was charged with calixV$_6$O$_6^{-1}$ (0.052 g, 0.033 mmol, 1.0 equiv), iodosylbenzene (0.011 g, 0.05 mmol, 1.4 equiv), and 6 mL of dichloromethane. The reaction mixture was heated to 45 °C with vigorous stirring for 2 h. After cooling to room temperature, the mixture was filtered over a glass pipet packed with a glass fiber filter paper, and the volatiles of the filtrate were removed under reduced pressure. The resulting brown-green solid was washed with a 3:1 mixture of diethyl ether/tetrahydrofuran (8 mL × 3). The remaining solid was recrystallized via slow diffusion of diethyl ether into a concentrated dichloromethane solution. The resulting crystalline material was washed with diethyl ether (2 mL × 2), and the remaining volatiles were removed under reduced pressure, affording calixV$_6$O$_7^{-1}$ as a dark, brown-green solid (0.035 g, 0.022 mmol, 65%). Crystals suitable for structural analysis were grown by layering a concentrated dichloromethane solution with toluene. ^{1}H NMR (400 MHz, CDCl$_3$): δ 28.04, 23.63, 21.52, 7.58 (arene), 1.21 (−CH$_2$− and *tert*-butyl). FT-IR (ATR, cm^{-1}): 1051 (O$_b$−CH$_3$), 961 (V═O$_t$). UV−vis (CH$_3$CN): 1000 nm (ε = 680 M^{-1} cm^{-1}). Elemental analysis for C$_{68}$H$_{112}$NO$_{19}$V$_6$·1/2 CH$_2$Cl$_2$ (MW = 1581.74 g/mol). Calculated (%): C, 51.97; H, 7.21; N, 0.97. Found (%): C, 52.02; H, 7.20; N, 0.89.

Activation of O$_2$ with calixV$_6$O$_6^{-1}$. In a glovebox, a 50 mL Schlenk flask was charged with 0.069 g of calixV$_6$O$_6^{-1}$ (44 μmol) and 6 mL of acetonitrile. The Schlenk flask was sealed, removed from the glovebox, and attached to a Schlenk line, where headspace was evacuated via three freeze−pump−thaw cycles. An atmosphere of O$_2$ was added to the flask, and the reaction was heated to 50 °C in an oil bath with rapid stirring. A gradual color change from brown to dark brown was observed. After 24 h, the reaction was cooled to room temperature, and the volatiles were removed under reduced pressure on a Schlenk line. The flask was returned to the glovebox, and the resulting residue was transferred from the flask to a 20 mL scintillation vial with dichloromethane. The dichloromethane was removed under reduced pressure. The residue was extracted with diethyl ether (4 mL × 4) and filtered, and the diethyl ether was removed under reduced pressure, affording calixV$_6$O$_6^0$ as a golden brown solid (0.017 g, 0.012 mmol, 28% based on calixV$_6$O$_6^{-1}$; characterization by ^{1}H NMR matches that of calixV$_6$O$_6^0$). ^{1}H NMR and CV analyses of the dark brown residue remaining after the diethyl ether extraction revealed a mixture of calixV$_6$O$_6^{-1}$ and calixV$_6$O$_7^{-1}$.

The CCDC has the supplementary crystallographic data for this paper: calixV$_6$O$_6^{-1}$, 2071335; calixV$_6$O$_7^{-1}$, 2071336.

■ ASSOCIATED CONTENT

Supporting Information

The Supporting Information is available free of charge at https://pubs.acs.org/doi/10.1021/acs.inorgchem.1c00887.

^{1}H NMR, ESI-MS, crystallographic parameters, and bond valence sum calculations as well as ^{1}H NMR of O$_2$ reduction reactions (PDF)

Accession Codes

CCDC 2071335−2071336 contain the supplementary crystallographic data for this paper. These data can be obtained free of charge via www.ccdc.cam.ac.uk/data_request/cif, or by emailing data_request@ccdc.cam.ac.uk, or by contacting The Cambridge Crystallographic Data Centre, 12 Union Road, Cambridge CB2 1EZ, UK; fax: +44 1223 336033.

■ AUTHOR INFORMATION

Corresponding Author

Ellen M. Matson − *Department of Chemistry, University of Rochester, Rochester, New York 14627, United States;* orcid.org/0000-0003-3753-8288; Email: matson@chem.rochester.edu

Authors

Rachel L. Meyer − *Department of Chemistry, University of Rochester, Rochester, New York 14627, United States*

Pere Miró − *Department of Chemistry, University of South Dakota, Vermillion, South Dakota 57069, United States;* orcid.org/0000-0002-3281-0708

William W. Brennessel − *Department of Chemistry, University of Rochester, Rochester, New York 14627, United States;* orcid.org/0000-0001-5461-1825

Complete contact information is available at: https://pubs.acs.org/10.1021/acs.inorgchem.1c00887

Author Contributions

The manuscript was written through contributions of all authors. All authors have given approval to the final version of the manuscript.

Notes

The authors declare no competing financial interest.

■ ACKNOWLEDGMENTS

This research was funded by the National Science Foundation (CHE-1653195). E.M.M. is a recipient of a Cottrell Award

from the Research Corporation for Science Advancement, which has provided additional resources to support this research.

■ REFERENCES

(1) Elstner, E. F. Oxygen activation and oxygen toxicity. *Annu. Rev. Plant Physiol.* **1982**, *33*, 73−96.
(2) Sawyer, D. T. *Oxygen Chemistry*; Oxford University Press, 1991; Vol. *26*.
(3) Punniyamurthy, T.; Velusamy, S.; Iqbal, J. Recent Advances in Transition Metal Catalyzed Oxidation of Organic Substrates with Molecular Oxygen. *Chem. Rev.* **2005**, *105*, 2329−2364.
(4) Shi, Z.; Zhang, C.; Tang, C.; Jiao, N. Recent advances in transition-metal catalyzed reactions using molecular oxygen as the oxidant. *Chem. Soc. Rev.* **2012**, *41*, 3381−3430.
(5) Babcock, G. T.; Wikström, M. Oxygen activation and the conservation of energy in cell respiration. *Nature* **1992**, *356*, 301−309.
(6) Wang, X.; Li, Z.; Qu, Y.; Yuan, T.; Wang, W.; Wu, Y.; Li, Y. Review of Metal Catalysts for Oxygen Reduction Reaction: From Nanoscale Engineering to Atomic Design. *Chem.* **2019**, *5*, 1486−1511.
(7) Morozan, A.; Jousselme, B.; Palacin, S. Low-platinum and platinum-free catalysts for the oxygen reduction reaction at fuel cell cathodes. *Energy Environ. Sci.* **2011**, *4*, 1238−1254.
(8) Liu, X.; Ryabenkova, Y.; Conte, M. Catalytic oxygen activation versus autoxidation for industrial applications: a physicochemical approach. *Phys. Chem. Chem. Phys.* **2015**, *17*, 715−731.
(9) Sui, S.; Wang, X.; Zhou, X.; Su, Y.; Riffat, S.; Liu, C.-j. A comprehensive review of Pt electrocatalysts for the oxygen reduction reaction: Nanostructure, activity, mechanism and carbon support in PEM fuel cells. *J. Mater. Chem. A* **2017**, *5*, 1808−1825.
(10) Campos-Martin, J. M.; Blanco-Brieva, G.; Fierro, J. L. G. Hydrogen Peroxide Synthesis: An Outlook beyond the Anthraquinone Process. *Angew. Chem., Int. Ed.* **2006**, *45*, 6962−6984.
(11) Sharma, S.; Goyal, P.; Maheshwari, S.; Chandra, A. A technical review of automobile catalytic converter: current status and perspectives. *Strategic Technologies of Complex Environmental Issues-A Sustainable Approach; Excellent Publishing House, 2014;* **2015**, *1*, 171−179.
(12) Trovarelli, A.; de Leitenburg, C.; Boaro, M.; Dolcetti, G. The utilization of ceria in industrial catalysis. *Catal. Today* **1999**, *50*, 353−367.
(13) Bañares, M. A. Supported metal oxide and other catalysts for ethane conversion: a review. *Catal. Today* **1999**, *51*, 319−348.
(14) Grant, J. T.; Venegas, J. M.; McDermott, W. P.; Hermans, I. Aerobic Oxidations of Light Alkanes over Solid Metal Oxide Catalysts. *Chem. Rev.* **2018**, *118*, 2769−2815.
(15) Védrine, J. C. Metal oxides in heterogeneous oxidation catalysis: State of the art and challenges for a more sustainable world. *ChemSusChem* **2019**, *12*, 577−588.
(16) Bielański, A.; Haber, J. Oxygen in catalysis on transition metal oxides. *Catal. Rev.: Sci. Eng.* **1979**, *19*, 1−41.
(17) Vedrine, J. C. *Metal Oxides in Heterogeneous Catalysis*; Elsevier, 2018.
(18) Ruiz Puigdollers, A.; Schlexer, P.; Tosoni, S.; Pacchioni, G. Increasing Oxide Reducibility: The Role of Metal/Oxide Interfaces in the Formation of Oxygen Vacancies. *ACS Catal.* **2017**, *7*, 6493−6513.
(19) Zhang, X.; Klabunde, K. J. Superoxide (O_2^-) on the surface of heat-treated ceria. Intermediates in the reversible oxygen to oxide transformation. *Inorg. Chem.* **1992**, *31*, 1706−1709.
(20) Kwapien, K.; Paier, J.; Sauer, J.; Geske, M.; Zavyalova, U.; Horn, R.; Schwach, P.; Trunschke, A.; Schlögl, R. Sites for Methane Activation on Lithium-Doped Magnesium Oxide Surfaces. *Angew. Chem., Int. Ed.* **2014**, *53*, 8774−8778.
(21) Mars, P.; van Krevelen, D. W. Oxidations carried out by means of vanadium oxide catalysts. *Chem. Eng. Sci.* **1954**, *3*, 41−59.
(22) Doornkamp, C.; Ponec, V. The universal character of the Mars and Van Krevelen mechanism. *J. Mol. Catal. A: Chem.* **2000**, *162*, 19−32.
(23) Diebold, U. The surface science of titanium dioxide. *Surf. Sci. Rep.* **2003**, *48*, 53−229.
(24) Ganduglia-Pirovano, M. V.; Hofmann, A.; Sauer, J. Oxygen vacancies in transition metal and rare earth oxides: Current state of understanding and remaining challenges. *Surf. Sci. Rep.* **2007**, *62*, 219−270.
(25) Brugnoli, L.; Pedone, A.; Menziani, M. C.; Adamo, C.; Labat, F. O_2 Activation over Ag-Decorated CeO_2(111) and TiO_2(110) Surfaces: A Theoretical Comparative Investigation. *J. Phys. Chem. C* **2020**, *124*, 25917−25930.
(26) Sun, S.; Li, C.; Zhang, D.; Wang, Y. Density functional theory study of the adsorption and dissociation of O_2 on CuO(111) surface. *Appl. Surf. Sci.* **2015**, *333*, 229−234.
(27) Wu, H.; Ma, S.; Song, W.; Hensen, E. J. M. Density Functional Theory Study of the Mechanism of Formaldehyde Oxidation on Mn-Doped Ceria. *J. Phys. Chem. C* **2016**, *120*, 13071−13077.
(28) Huang, M.; Fabris, S. Role of surface peroxo and superoxo species in the low-temperature oxygen buffering of ceria: Density functional theory calculations. *Phys. Rev. B: Condens. Matter Mater. Phys.* **2007**, *75*, 081404.
(29) Bigi, C.; Tang, Z.; Pierantozzi, G. M.; Orgiani, P.; Das, P. K.; Fujii, J.; Vobornik, I.; Pincelli, T.; Troglia, A.; Lee, T.-L.; Ciancio, R.; Drazic, G.; Verdini, A.; Regoutz, A.; King, P. D. C.; Biswas, D.; Rossi, G.; Panaccione, G.; Selloni, A. Distinct behavior of localized and delocalized carriers in anatase TiO_2(001) during reaction with O_2. *Physical Review Materials* **2020**, *4*, 025801.
(30) Shoko, E.; Smith, M.; McKenzie, R. H. Charge distribution near bulk oxygen vacancies in cerium oxides. *J. Phys.: Condens. Matter* **2010**, *22*, 223201.
(31) López, X.; Carbó, J. J.; Bo, C.; Poblet, J. M. Structure, properties and reactivity of polyoxometalates: a theoretical perspective. *Chem. Soc. Rev.* **2012**, *41*, 7537−7571.
(32) Gumerova, N. I.; Rompel, A. Synthesis, structures and applications of electron-rich polyoxometalates. *Nature Reviews Chemistry* **2018**, *2*, 0112.
(33) Pope, M. T.; Müller, A. Introduction to Polyoxometalate Chemistry: From Topology *via* Self-assembly to Applications. In *Polyoxometalate Chemistry From Topology via Self-Assembly to Applications*; Pope, M. T., Müller, A., Eds.; Springer Netherlands: Dordrecht, 2001; pp 1−6.
(34) Long, D.-L.; Tsunashima, R.; Cronin, L. Polyoxometalates: Building Blocks for Functional Nanoscale Systems. *Angew. Chem., Int. Ed.* **2010**, *49*, 1736−1758.
(35) Anderson, T. M.; Hill, C. L. Modeling Reactive Metal Oxides. Kinetics, Thermodynamics, and Mechanism of M_3 Cap Isomerization in Polyoxometalates. *Inorg. Chem.* **2002**, *41*, 4252−4258.
(36) Lechner, M.; Güttel, R.; Streb, C. Challenges in polyoxometalate-mediated aerobic oxidation catalysis: catalyst development meets reactor design. *Dalton Transactions* **2016**, *45*, 16716−16726.
(37) Kholdeeva, O. A.; Maksimovskaya, R. I. Titanium- and zirconium-monosubstituted polyoxometalates as molecular models for studying mechanisms of oxidation catalysis. *J. Mol. Catal. A: Chem.* **2007**, *262*, 7−24.
(38) Harrup, M. K.; Hill, C. L. Polyoxometalate Catalysis of the Aerobic Oxidation of Hydrogen Sulfide to Sulfur. *Inorg. Chem.* **1994**, *33*, 5448−5455.
(39) Wang, S.-S.; Yang, G.-Y. Recent Advances in Polyoxometalate-Catalyzed Reactions. *Chem. Rev.* **2015**, *115*, 4893−4962.
(40) Kholdeeva, O. A.; Vanina, M. P.; Timofeeva, M. N.; Maksimovskaya, R. I.; Trubitsina, T. A.; Melgunov, M. S.; Burgina, E. B.; Mrowiec-Bialon, J.; Jarzebski, A. B.; Hill, C. L. Co-containing polyoxometalate-based heterogeneous catalysts for the selective aerobic oxidation of aldehydes under ambient conditions. *J. Catal.* **2004**, *226*, 363−371.
(41) Bar-Nahum, I.; Khenkin, A. M.; Neumann, R. Mild, Aqueous, Aerobic, Catalytic Oxidation of Methane to Methanol and

Acetaldehyde Catalyzed by a Supported Bipyrimidinylplatinum−Polyoxometalate Hybrid Compound. *J. Am. Chem. Soc.* **2004**, *126*, 10236−10237.
(42) Kholdeeva, O. A.; Timofeeva, M. N.; Maksimov, G. M.; Maksimovskaya, R. I.; Neiwert, W. A.; Hill, C. L. Aerobic Oxidation of Formaldehyde Mediated by a Ce-Containing Polyoxometalate under Mild Conditions. *Inorg. Chem.* **2005**, *44*, 666−672.
(43) Weinstock, I. A.; Schreiber, R. E.; Neumann, R. Dioxygen in Polyoxometalate Mediated Reactions. *Chem. Rev.* **2018**, *118* (5), 2680−2717.
(44) Duncan, D. C.; Hill, C. L. Mechanism of Reaction of Reduced Polyoxometalates with O_2 Evaluated by ^{17}O NMR. *J. Am. Chem. Soc.* **1997**, *119*, 243−244.
(45) Geletii, Y. V.; Hill, C. L.; Atalla, R. H.; Weinstock, I. A. Reduction of O2 to Superoxide Anion ($O_2^{\bullet-}$) in Water by Heteropolytungstate Cluster-Anions. *J. Am. Chem. Soc.* **2006**, *128*, 17033−17042.
(46) Snir, O.; Wang, Y.; Tuckerman, M. E.; Geletii, Y. V.; Weinstock, I. A. Concerted Proton−Electron Transfer to Dioxygen in Water. *J. Am. Chem. Soc.* **2010**, *132*, 11678−11691.
(47) Efremenko, I.; Neumann, R. Computational Insight into the Initial Steps of the Mars−van Krevelen Mechanism: Electron Transfer and Surface Defects in the Reduction of Polyoxometalates. *J. Am. Chem. Soc.* **2012**, *134*, 20669−20680.
(48) Khenkin, A. M.; Efremenko, I.; Martin, J. M. L.; Neumann, R. The kinetics and mechanism of oxidation of reduced phosphovanadomolybdates by molecular oxygen: theory and experiment in concert. *Phys. Chem. Chem. Phys.* **2018**, *20*, 7579−7587.
(49) Khenkin, A. M.; Neumann, R. Low-Temperature Activation of Dioxygen and Hydrocarbon Oxidation Catalyzed by a Phosphovanadomolybdate: Evidence for a Mars−van Krevelen Type Mechanism in a Homogeneous Liquid Phase. *Angew. Chem., Int. Ed.* **2000**, *39*, 4088−4090.
(50) Khenkin, A. M.; Weiner, L.; Wang, Y.; Neumann, R. Electron and Oxygen Transfer in Polyoxometalate, $H_5PV_2Mo_{10}O_{40}$, Catalyzed Oxidation of Aromatic and Alkyl Aromatic Compounds: Evidence for Aerobic Mars−van Krevelen-Type Reactions in the Liquid Homogeneous Phase. *J. Am. Chem. Soc.* **2001**, *123*, 8531−8542.
(51) Neumann, R.; Khenkin, A. M. Molecular oxygen and oxidation catalysis by phosphovanadomolybdates. *Chem. Commun.* **2006**, 2529−2538.
(52) Petel, B. E.; Brennessel, W. W.; Matson, E. M. Oxygen-Atom Vacancy Formation at Polyoxovanadate Clusters: Homogeneous Models for Reducible Metal Oxides. *J. Am. Chem. Soc.* **2018**, *140*, 8424−8428.
(53) Petel, B. E.; Matson, E. M. Conversion of NO_x^{1-} (x = 2, 3) to NO using an oxygen-deficient polyoxovanadate−alkoxide cluster. *Chem. Commun.* **2020**, *56*, 555−558.
(54) Petel, B. E.; Matson, E. M., Physicochemical Factors That Influence the Deoxygenation of Oxyanions in Atomically Precise, Oxygen-Deficient Vanadium Oxide Assemblies. *Inorg. Chem.* **2021**.*606855*
(55) Cozzolino, A. F.; Tofan, D.; Cummins, C. C.; Temprado, M.; Palluccio, T. D.; Rybak-Akimova, E. V.; Majumdar, S.; Cai, X.; Captain, B.; Hoff, C. D. Two-Step Binding of O_2 to a Vanadium(III) Trisanilide Complex To Form a Non-Vanadyl Vanadium(V) Peroxo Complex. *J. Am. Chem. Soc.* **2012**, *134*, 18249−18252.
(56) Liu, Z.; Anson, F. C. Schiff base complexes of vanadium (III, IV, V) as catalysts for the electroreduction of O_2 to H_2O in acetonitrile. *Inorg. Chem.* **2001**, *40*, 1329−1333.
(57) Barroso, S.; Coelho, A. M.; Adão, P.; Calhorda, M. J.; Martins, A. M. Radical reactions of diamine bis(phenolate) vanadium(iii) complexes. Solid state binding of O_2 to form a vanadium(v) peroxo complex. *Dalton Transactions* **2017**, *46*, 9692−9704.
(58) Aronica, C.; Chastanet, G.; Zueva, E.; Borshch, S. A.; Clemente-Juan, J. M.; Luneau, D. A Mixed-Valence Polyoxovanadate-(III,IV) Cluster with a Calixarene Cap Exhibiting Ferromagnetic V(III)−V(IV) Interactions. *J. Am. Chem. Soc.* **2008**, *130* (7), 2365−2371.
(59) Breslow, R.; Dong, S. D. Biomimetic Reactions Catalyzed by Cyclodextrins and Their Derivatives. *Chem. Rev.* **1998**, *98*, 1997−2012.
(60) Gramage-Doria, R.; Armspach, D.; Matt, D. Metallated cavitands (calixarenes, resorcinarenes, cyclodextrins) with internal coordination sites. *Coord. Chem. Rev.* **2013**, *257*, 776−816.
(61) Le Poul, N.; Le Mest, Y.; Jabin, I.; Reinaud, O. Supramolecular Modeling of Mono-copper Enzyme Active Sites with Calix[6]arene-based Funnel Complexes. *Acc. Chem. Res.* **2015**, *48*, 2097−2106.
(62) De Leener, G.; Over, D.; Smet, C.; Cornut, D.; Porras-Gutierrez, A. G.; López, I.; Douziech, B.; Le Poul, N.; Topić, F.; Rissanen, K.; Le Mest, Y.; Jabin, I.; Reinaud, O. Two-Story" Calix[6]arene-Based Zinc and Copper Complexes: Structure, Properties, and O_2 Binding. *Inorg. Chem.* **2017**, *56*, 10971−10983.
(63) Izzet, G.; Zeitouny, J.; Akdas-Killig, H.; Frapart, Y.; Ménage, S.; Douziech, B.; Jabin, I.; Le Mest, Y.; Reinaud, O. Dioxygen Activation at a Mononuclear Cu(I) Center Embedded in the Calix[6]arene-Tren Core. *J. Am. Chem. Soc.* **2008**, *130*, 9514−9523.
(64) Castellano, B.; Solari, E.; Floriani, C.; Re, N.; Chiesi-Villa, A.; Rizzoli, C. The Chemistry of Vanadium−Carbon Bond Functionalities over an Oxo-Surface Defined by the Calix[4]arene Skeleton: The Redox Relationship between Vanadium(III) and Vanadium(IV) Assisted by Carbon−Oxygen Bond Cleavage. *Organometallics* **1998**, *17*, 2328−2336.
(65) Petel, B. E.; Fertig, A. A.; Maiola, M. L.; Brennessel, W. W.; Matson, E. M. Controlling Metal-to-Oxygen Ratios via M═O Bond Cleavage in Polyoxovanadate Alkoxide Clusters. *Inorg. Chem.* **2019**, *58*, 10462−10471.
(66) Petel, B. E.; Meyer, R. L.; Brennessel, W. W.; Matson, E. M. Oxygen atom transfer with organofunctionalized polyoxovanadium clusters: O-atom vacancy formation with tertiary phosphanes and deoxygenation of styrene oxide. *Chemical Science* **2019**, *10*, 8035−8045.
(67) Daniel, C.; Hartl, H. Neutral and Cationic V^{IV}/V^{V} Mixed-Valence Alkoxo-polyoxovanadium Clusters $[V_6O_7(OR)_{12}]^{n+}$ (R = $-CH_3$, $-C_2H_5$): Structural, Cyclovoltammetric and IR-Spectroscopic Investigations on Mixed Valency in a Hexanuclear Core. *J. Am. Chem. Soc.* **2005**, *127*, 13978−13987.
(68) Daniel, C.; Hartl, H. A Mixed-Valence V^{IV}/V^{V} Alkoxo-polyoxovanadium Cluster Series $[V_6O_8(OCH_3)_{11}]^{n\pm}$: Exploring the Influence of a μ-Oxo Ligand in a Spin Frustrated Structure. *J. Am. Chem. Soc.* **2009**, *131*, 5101−5114.
(69) Li, F.; Carpenter, S. H.; Higgins, R. F.; Hitt, M. G.; Brennessel, W. W.; Ferrier, M. G.; Cary, S. K.; Lezama-Pacheco, J. S.; Wright, J. T.; Stein, B. W.; Shores, M. P.; Neidig, M. L.; Kozimor, S. A.; Matson, E. M. Polyoxovanadate−Alkoxide Clusters as a Redox Reservoir for Iron. *Inorg. Chem.* **2017**, *56*, 7065−7080.
(70) Spandl, J.; Daniel, C.; Brüdgam, I.; Hartl, H. Synthesis and Structural Characterization of Redox-Active Dodecamethoxoheptaoxohexavanadium Clusters. *Angew. Chem., Int. Ed.* **2003**, *42*, 1163−1166.
(71) D'Alessandro, D. M.; Keene, F. R. A cautionary warning on the use of electrochemical measurements to calculate comproportionation constants for mixed-valence compounds. *Dalton Transactions* **2004**, 3950−3954.
(72) Sutton, J. E.; Sutton, P. M.; Taube, H. Determination of the comproportionation constant for a weakly coupled mixed-valence system by titration of the intervalence transfer band: μ-(4,4′-bipyridyl)-bis(pentaammineruthenium)(5+). *Inorg. Chem.* **1979**, *18*, 1017−1021.
(73) Ward, M. D. Metal-metal interactions in binuclear complexes exhibiting mixed valency; molecular wires and switches. *Chem. Soc. Rev.* **1995**, *24*, 121−134.
(74) Caselli, A.; Solari, E.; Scopelliti, R.; Floriani, C.; Re, N.; Rizzoli, C.; Chiesi-Villa, A. Dinitrogen Rearranging over a Metal−Oxo Surface and Cleaving to Nitride: From the End-On to the Side-On Bonding Mode, to the Stepwise Cleavage of the N⋮N Bonds Assisted by Nb^{III}-calix[4]arene. *J. Am. Chem. Soc.* **2000**, *122*, 3652−3670.

(75) Redshaw, C. Coordination chemistry of the larger calixarenes. *Coord. Chem. Rev.* **2003**, *244*, 45−70.
(76) Floriani, C.; Floriani-Moro, R. The MC bond functionalities bonded to an oxo-surface modeled by Calix[4]arenes. In *Advanced Organometallic Chemistry*; Academic Press, 2001; Vol. *47*, pp 167−233.
(77) Castellano, B.; Solari, E.; Floriani, C.; Scopelliti, R.; Re, N. Reactivity of a Vanadium(III) Center over an Oxo Surface Modeled by Calix[4]arene. *Inorg. Chem.* **1999**, *38*, 3406−3413.
(78) Hänninen, M. M.; Peuronen, A.; Damlin, P.; Tyystjärvi, V.; Kivelä, H.; Lehtonen, A. Vanadium complexes with multidentate amine bisphenols. *Dalton Transactions* **2014**, *43*, 14022−14028.
(79) Yousef Ebrahimipour, S.; Mague, J. T.; Akbari, A.; Takjoo, R. Synthesis, characterization, crystal structure and thermal behavior of 4-Bromo-2-(((5-chloro-2-hydroxyphenyl)imino)methyl)phenol and its oxido-vanadium(V) complexes. *J. Mol. Struct.* **2012**, *1028*, 148−155.
(80) Monfared, H. H.; Alavi, S.; Bikas, R.; Vahedpour, M.; Mayer, P. Vanadiumoxo−aroylhydrazone complexes: Synthesis, structure and DFT calculations. *Polyhedron* **2010**, *29*, 3355−3362.
(81) Gazi, S.; Đokić, M.; Moeljadi, A. M. P.; Ganguly, R.; Hirao, H.; Soo, H. S. Kinetics and DFT Studies of Photoredox Carbon−Carbon Bond Cleavage Reactions by Molecular Vanadium Catalysts under Ambient Conditions. *ACS Catal.* **2017**, *7*, 4682−4691.
(82) Wichmann, O.; Sopo, H.; Lehtonen, A.; Sillanpää, R. Oxidovanadium(V) Complexes with Aminoethanol Bis(phenolate) [O,N,O,O′] Ligands: Preparations, Structures, N-Dealkylation and Condensation Reactions. *Eur. J. Inorg. Chem.* **2011**, *2011*, 1283−1291.
(83) Hoppe, E.; Limberg, C.; Ziemer, B. Mono- and Dinuclear Oxovanadium(V)calixarene Complexes and Their Activity as Oxidation Catalysts. *Inorg. Chem.* **2006**, *45*, 8308−8317.
(84) VanGelder, L. E.; Kosswattaarachchi, A. M.; Forrestel, P. L.; Cook, T. R.; Matson, E. M. Polyoxovanadate-alkoxide clusters as multi-electron charge carriers for symmetric non-aqueous redox flow batteries. *Chemical Science* **2018**, *9*, 1692−1699.
(85) Gutsche, C. D.; Iqbal, M. *p*-tert-butylcalix[4]arene. *Org. Synth.* **1990**, *68*, 234.

https://doi.org/10.1021/acs.inorgchem.1c00887
Inorg. Chem. 2021, 60, 13833−13843